Supplementary information for "A silicon-based single-electron interferometer coupled to a fermionic sea "

Anasua Chatterjee,[1] Sergey N. Shevchenko,[2,3,4] Sylvain Barraud,[5] Rubén M. Otxoa,[6,7] Franco Nori,[2,8] John J. L. Morton,[1,9] and M. Fernando Gonzalez-Zalba[6]

[1]*London Centre for Nanotechnology, University College London, London, WC1H 0AH, United Kingdom*

[2]*Center for Emergent Matter Science, RIKEN, Wako-shi, Saitama 351-0198, Japan*

[3]*B. Verkin Institute for Low Temperature Physics and Engineering, Kharkov 61103, Ukraine*

[4]*V. Kazarin Kharkov National University, Kharkov 61022, Ukraine*

[5]*CEA/LETI-MINATEC, CEA-Grenoble, 38000 Grenoble, France*

[6]*Hitachi Cambridge Laboratory, J. J. Thomson Avenue, Cambridge CB3 0HE, United Kingdom*

[7]*Donostia International Physics Center, Donostia-San Sebastian 20018, Spain*

[8]*Physics Department, University of Michigan, Ann Arbor, MI 48109-1040, USA*

[9]*Department of Electronic & Electrical Engineering, University College London, London WC1E 7JE, United Kingdom*

1. MAGNETO-SPECTROSCOPY AND DETERMINATION OF GATE COUPLINGS

In this section, we discuss the calculation of the gate couplings α_{L} and α_{R} defined as the ratio between the gate capacitance $C_{\mathrm{g1(2)}}$ and the total capacitance $C_{\Sigma 1(2)}$ for the left (right) dot. This can be done by looking at an absolute energy scale of the system, for example, the Zeeman splitting. In our case, we use magneto-spectroscopy [1]. We monitor the position in top-gate voltage of the (10)-(11) dot-to-sea transition (DST) shown in Fig. 1(c) in the main text, while sweeping the magnetic field [Fig. S1]. The shift in the peak location, ΔV_{TG}, towards a lower top-gate voltage, as a function of the magnetic field B, gives a calibration of the top-gate coupling to the right dot, $\alpha_{\mathrm{R}} = g\mu_{\mathrm{B}}B/\Delta V_{\mathrm{TG}} = 0.86$, where g is the electron g-factor and μ_{B} is the Bohr magneton. To obtain the top-gate coupling to the left dot, α_{L}, we use the fact that, in the multi-passage LZSM regime, interference fringes appear at equidistant values of the top-gate voltage given by the equation $\delta V_{\mathrm{TG}} = hf_{\mathrm{mw}}/2e\alpha_{-}$ [as seen in Fig. 3(c) in the main text]. We obtain $\alpha_{\mathrm{L}} = 0.96$. This calculation also enables us to calibrate to energy the ε_0 axis in Fig. 2(b), for example. We also calibrate the microwave source voltage output V_{mw}, to microwave energy amplitude A_{mw}, using the condition that, at the edge of the LZSM interference region in Fig. 3(c) in the main text, $A_{\mathrm{mw}} = \varepsilon_0$.

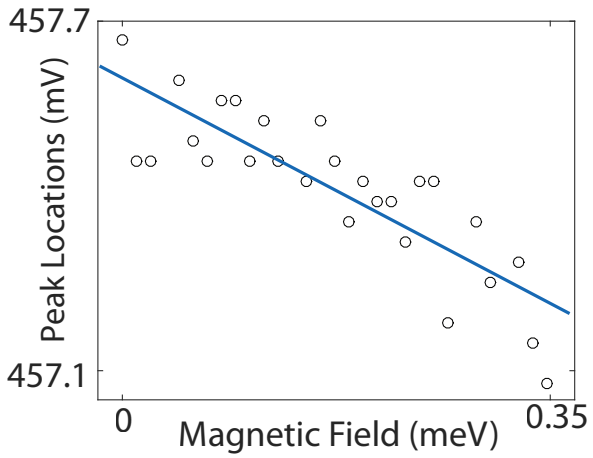

FIG. S1. Peak position in top-gate voltage plotted against the magnetic field energy [assuming $g = 2$ (black hollow circles)] and linear fit to the data (blue solid line).

2. CALCULATION OF THE ENERGY SPECTRUM

We calculate the energy spectrum of the double quantum dot system $\Delta E(N_1, N_2)$, where N_1 and N_2 are the charges in the left and right dot respectively, extending the results from Ref. [2]

$$\begin{aligned}\Delta E(N_1,N_2) = &\frac{1}{2}N_1^2E_{\mathrm{C1}} + \frac{1}{2}N_2^2E_{\mathrm{C2}} + N_1N_2E_{\mathrm{Cm}} \\ &- \frac{1}{|e|}\left\{C_{\mathrm{g1}}V_{\mathrm{TG}}(N_1E_{\mathrm{C1}} + N_2E_{\mathrm{Cm}}) + C_{\mathrm{g2}}V_{\mathrm{TG}}(N_1E_{\mathrm{Cm}} + N_2E_{\mathrm{C2}})\right. \\ &\left.+C_{\mathrm{b1}}V_{\mathrm{BG}}(N_1E_{\mathrm{C1}} + N_2E_{\mathrm{Cm}}) + C_{\mathrm{b2}}V_{\mathrm{BG}}(N_1E_{\mathrm{Cm}} + N_2E_{\mathrm{C2}})\right\} \\ &+ \frac{1}{e^2}\left\{\frac{1}{2}C_{\mathrm{g1}}^2V_{\mathrm{g}}^2E_{\mathrm{C1}} + \frac{1}{2}C_{\mathrm{g2}}^2V_{\mathrm{g}}^2E_{\mathrm{C2}} + C_{\mathrm{g1}}C_{\mathrm{g2}}V_{\mathrm{g}}^2E_{\mathrm{Cm}}\right. \\ &\left.+\frac{1}{2}C_{\mathrm{b1}}^2V_{\mathrm{BG}}^2E_{\mathrm{C1}} + \frac{1}{2}C_{\mathrm{b2}}^2V_{\mathrm{BG}}^2E_{\mathrm{C2}} + C_{\mathrm{b1}}C_{\mathrm{b2}}V_{\mathrm{BG}}^2E_{\mathrm{Cm}}\right\}.\end{aligned} \tag{1}$$

where the various parameters of the double-dot system are described by the simplified circuit diagram shown in Fig. S2. In Eq. 1, E_{C1}, E_{C1} and E_{Cm} correspond to the charging energy of the left dot, right dot and mutual energy, respectively.

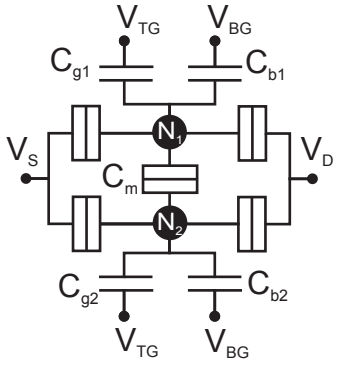

FIG. S2. Circuit diagram for a double quantum dot system, with gate couplings modelled as capacitances. Here, N_1 and N_2 indicate the electron number in each dot, respectively. The applied voltages are indicated with a V, with an appropriate subscript.

In order to simplify the expression, we define several new variables. We introduce the reduced top-gate and back-gate voltages, n_{t} and n_{b}, respectively,

$$\begin{aligned} n_{\mathrm{t}} &= \frac{C_{\mathrm{g1}} V_{\mathrm{TG}}}{|e|} \\ n_{\mathrm{b}} &= \frac{C_{\mathrm{b1}} V_{\mathrm{BG}}}{|e|}. \end{aligned} \tag{2}$$

Additionally, we consider the following approximate charging energy relation

$$E_{\mathrm{C}} = E_{\mathrm{C1}} = E_{\mathrm{C2}} = m E_{\mathrm{Cm}}, \tag{3}$$

where m accounts for the ratio between the charging energy and mutual energy. Moreover, we may introduce the asymmetry in the gate couplings a defined by:

$$a = \frac{2\,|\alpha_-|}{\max(\alpha_{\mathrm{L}}, \alpha_{\mathrm{R}})}. \tag{4}$$

where $\alpha_- = (\alpha_{\mathrm{L}} - \alpha_{\mathrm{R}})/2$. We can now express the ratio of the DQD energies to the total charging energy as

$$\begin{aligned} \frac{\Delta E(N_1, N_2)}{E_C} = & \frac{1}{2}N_1^2 + \frac{1}{2}N_2^2 + \frac{N_1 N_2}{m} \\ & - n_t \left\{ N_1 + \frac{N_2}{m} + (1+a)\left(\frac{N_1}{m} + N_2\right) \right\} \\ & - n_b \left\{ N_1 + \frac{N_2}{m} + (1-a)\left(\frac{N_1}{m} + N_2\right) \right\} \\ & - n_t^2 \left\{ \frac{1}{2} + \frac{1}{2}(1+a)^2 + \frac{1+a}{m} \right\} \\ & - n_b^2 \left\{ \frac{1}{2} + \frac{1}{2}(1-a)^2 + \frac{1-a}{m} \right\}. \end{aligned} \tag{5}$$

We find that the reduced back-gate voltage value at which we perform the experiment – the middle of the ICT line – corresponds to $n_{\mathrm{b}}^0 = 0.25$. Finally, we calculate the reduced-energy diagram of the DQD across the $n_{\mathrm{b}} = 0.25$ line, as shown in Fig. 2(a) in the main text. We do so by plotting $\Delta E/E_{\mathrm{C}}(N_1, N_2)$ for $N_1, N_2 = 0, 1$ as a function of reduced detuning $\varepsilon_0/E_{\mathrm{C}} = 2\alpha_- n_{\mathrm{t}}/\alpha_{\mathrm{L}}$, for $m = 10$ and $a = 0.1$, as in the case of the experiment. We use a tunnel coupling $\Delta_{\mathrm{c}} = E_{\mathrm{C}}/150$.

3. FREQUENCY DEPENDENCE OF THE LZSM INTERFERENCE PATTERN

The microwave frequency used to drive the LZSM experiment can have a significant effect on the interference pattern, depending on the qubit timescales. If the microwave

frequency is lowered below the electron phase coherence time T_2, the system goes into the incoherent regime, where the electron phase coherence is lost before two consecutive passages are performed. In our double quantum dot, T_2 can therefore be studied by performing a microwave-frequency dependence of the LZSM interferometry pattern. Figure S3 shows the LZSM interferometry results obtained using two different microwave frequencies (4.72 GHz and 4 GHz). In (a), taken at 4.72 GHz, we observe a few lines of interference in the double-passage region, indicating that $f_{\rm mw}^{-1}$ is approaching T_2. In (b), taken at 4 GHz, there are almost no visible interference fringes indicating $f_{\rm mw}^{-1} \simeq T_2$. Below 4 GHz the interference pattern disappears, indicating that we have an upper limit of $T_2 \simeq 250$ ps.

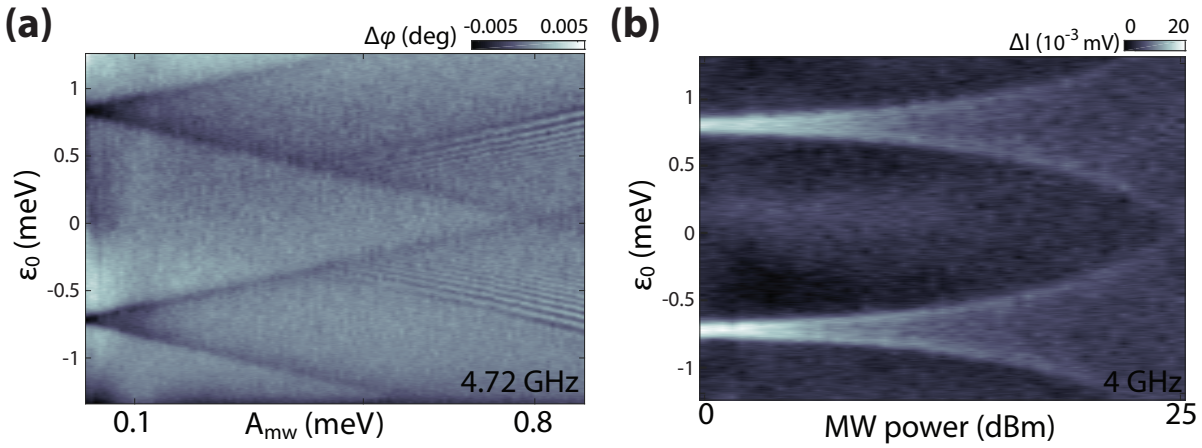

FIG. S3. (a) Resonator phase response as a function of detuning ϵ_0 and the microwave amplitude at (a) 4.72 GHz (b) In-phase component of the resonator response at 4 GHz, showing the decline and disappearance of the LZSM interference pattern.

4. STUCKELBERG PHASE FOR THE DOUBLE-PASSAGE EXPERIMENT

The Stückelberg phase, $\phi_{\rm St}$, that encapsulates the phase difference acquired after the first passage, can be derived in the adiabatic-impulse model by considering a driven two-level system [3]. In the fast-passage limit ($\Delta_{\rm c}^2/A_{\rm mw}\omega < 1$), the upper-level probability after two passages reads,

$$P_{\mathrm{doub}} \simeq 2\pi \frac{\Delta_{\mathrm{c}}^2}{A_{\mathrm{mw}}\omega} \left(1 - \frac{\varepsilon_0^2}{A_{\mathrm{mw}}^2}\right)^{-1/2} \sin^2 \phi_{\mathrm{St}}, \tag{6}$$

$$\phi_{\mathrm{St}} = -\frac{\varepsilon_0}{\omega} \arccos\left(\frac{\varepsilon_0}{A_{\mathrm{mw}}}\right) + \frac{A_{\mathrm{mw}}}{\omega}\left(1 - \frac{\varepsilon_0^2}{A_{\mathrm{mw}}^2}\right)^{1/2} - \frac{\pi}{4} \tag{7}$$

where $\omega = 2\pi f_{\mathrm{mw}}$. Equation (6) can be simplified in leading order with $\varepsilon_0/A_{\mathrm{mw}}$:

$$P_{\mathrm{double}} \simeq \frac{2\pi}{\omega} \frac{\Delta_{\mathrm{c}}^2}{A_{\mathrm{mw}}} \sin^2\left[\frac{A_{\mathrm{mw}}}{\omega} - \frac{\pi}{2}\frac{\varepsilon_0}{\omega} - \frac{\pi}{4}\right]. \tag{8}$$

Finally, we use this expression to calculate the dispersive response of the resonator in Fig. 4(c) in the main text. We note that both the amplitude and frequency dependence in Eq. (8) is in agreement with the result of Ref. [4] in the linear approximation. And this didactic result comes as a nice surprise, since the latter result was obtained in the assumption of small Δ_{c} and fast and strong driving, while the former result was obtained in the LZSM picture of adiabatic-impulse model, with impulse-type transitions between adiabatic energy levels.

5. INCOHERENT REGIME

In this section, we calculate the resonator response $\Delta\varphi$ in the incoherent regime, when single-electrons are exchanged at microwave frequencies between the left (or right) QD and the source and drain reservoirs. This scenario can be accurately described by a fast-driven two-level system [5, 6]. In this situation, we calculate the parametric capacitance of a single QD, given by the expression,

$$C_{\mathrm{pm}} = -\left(e\alpha_{\mathrm{L}}\right)^2 \frac{\partial \overline{P_1}(t)}{\partial \varepsilon_0}. \tag{9}$$

where $\overline{P_1}$ is the average probability of having one excess electron in the left QD. Also, $\overline{P_1}$ can be calculated from the time-dependent expression of the probability subject to a sinusoidal change in energy detuning $\varepsilon(t) = \varepsilon_0 + A_{\mathrm{mw}}\sin(2\pi f_{\mathrm{mw}} t)$ induced by a microwave electric field with amplitude A_{mw} and frequency f_{mw} around an energy detuning offset ε_0,

$$P_1(t) \simeq \frac{1}{1 + \exp\left(\frac{\varepsilon(t)}{k_{\mathrm{B}}T}\right)} \tag{10}$$

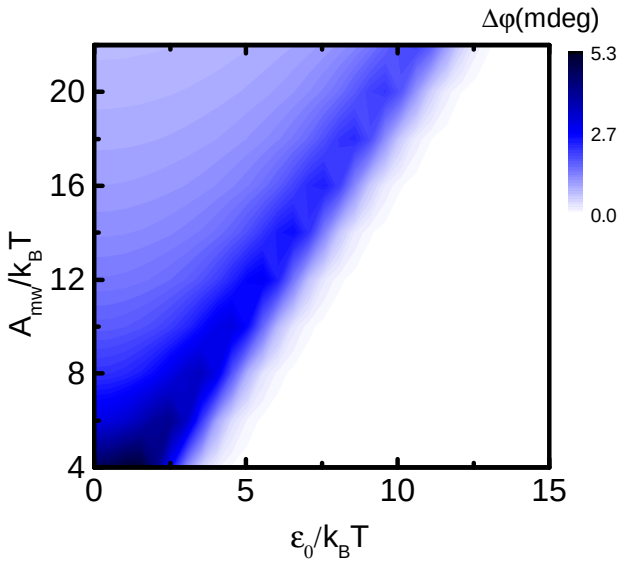

FIG. S4. Resonator phase response $\Delta\varphi$ as a function of reduced detuning $\varepsilon_0/k_{\mathrm{B}}T$ and reduced microwave amplitude $A_{\mathrm{mw}}/k_{\mathrm{B}}T$

where k_{B} is the Boltzmann constant and T the electron temperature. In Fig S4, we present the resonator phase response as a function of ε_0 and A_{mw}, for a resonator quality factor $Q = 42$, $\alpha_{\mathrm{L}} = 0.96$, and $T = 100$ mK. The calculation matches well the data in Fig. 2(b) (blue-star regions). Particularly, it captures the enhancement of the phase signal at $\varepsilon_0 = A_{\mathrm{mw}}$.

6. RELAXATION RATES FOR THE DOT-TO-LEAD TRANSITIONS

In this section, we provide a quantitative analysis of the relaxation rates between the left (right) dot and the electron reservoirs, Γ_{L} (Γ_{R}). As discussed in the main text, the difference in these relaxation rates results in relaxation occurring primarily at the (01)-(11) and (00)-(10) DSTs rather than at the (00)-(01) and (10)-(11) transitions when operating the system in the strong driving regime. This can be directly observed in Fig. 2(b) of the main text, where no additional observable change in $\Delta\varphi$ appears in the regions $A_{\mathrm{mw}} < \left|\varepsilon_0 - \varepsilon_0^{00-01}\right|$ and $A_{\mathrm{mw}} < \left|\varepsilon_0 - \varepsilon_0^{10-11}\right|$, where ε_0^{00-01} and ε_0^{10-11} correspond to the position in detuning of the (00)-(01) and (10)-(11) crossings, respectively. In the following, we provide additional experimental evidence demonstrating that $\Gamma_{\mathrm{L}} \gg \Gamma_{\mathrm{R}}$.

First, we extract Γ_{L}. For the (01)-(11) DST, the probability of an electron in the left dot to relax into the source-drain reservoir is given by $P_{\mathrm{SD}} = 1 - \exp\left(-\Gamma_{\mathrm{L}}\Delta t\right)$, where the Δt is the time the electron spends at a value of detuning larger than the position of the (01)-(11) crossing (ε_0^{01-11}). It can be shown that

$$\Delta t = \frac{\pi}{\omega} - \frac{2}{\omega}\sin^{-1}\left(\frac{\varepsilon_0^{01-11} - \varepsilon_0}{A_{\mathrm{mw}}}\right) = \frac{1}{\omega}\left[\pi - 2\sin^{-1}(\frac{\varepsilon_0^{01-11} - \varepsilon_0}{A_{\mathrm{mw}}})\right], \tag{11}$$

which then gives

$$P_{\mathrm{SD}} = 1 - \exp\left\{\frac{-\Gamma_{\mathrm{L}}}{\omega}\left[\pi - 2\sin^{-1}\left(\frac{\varepsilon_0^{01-11} - \varepsilon_0}{A_{\mathrm{mw}}}\right)\right]\right\}. \tag{12}$$

Since in the double-passage regime, the probability P_{11} is proportional to P_{SD}, we fit Eq. (12) to the envelope of the oscillations (which decay along detuning axis as predicted by the equation), as shown in Fig. S5(a), for a trace taken at $f_{\mathrm{mw}} = 15\,\mathrm{GHz}$. The fit gives a tunnel rate of $\Gamma_{\mathrm{L}} \approx 50\,\mathrm{GHz}$.

To extract Γ_{R}, we perform an analysis of the temperature dependence of (10)-(11) DTS. In Fig. S5, we show the FWHM of the $\Delta\varphi$ peak as a function of the temperature of the mixing chamber. As we lower the temperature, we see a linear decrease of the FWHM until 700 mK. Decreasing the temperature further leads to a saturation of the FHWM to 100 μeV below 200 mK. The mechanism that can lead to saturation of the FWHM can be originated by either electron-phonon decoupling or lifetime broadening [7]. In the case of electron-phonon decoupling, the saturation occurs at FWHM$= 3.5k_{\mathrm{B}}T$ and in the case of lifetime-broadening FWHM$= 2h\Gamma_{\mathrm{R}}$. From the data, we are unable to distinguish the exact mechanism that causes saturation but we can extract an upper bound for $\Gamma_{\mathrm{R}} < 12$ GHz.

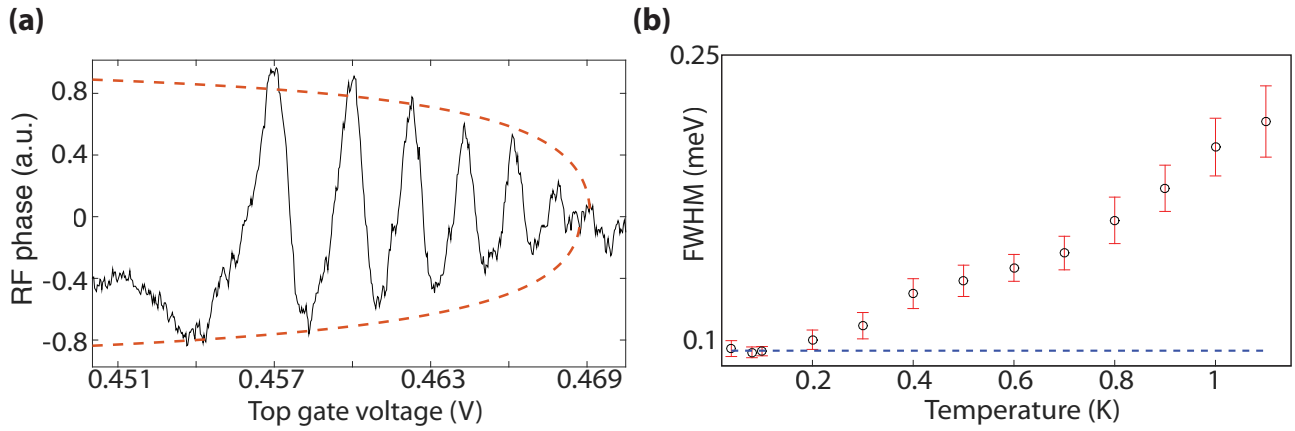

FIG. S5. (a) Resonator phase response as a function of top gate voltage V_{TG}, with a fit to the envelope of the oscillations as given by Eq. 12. (b) Full width at half maximum of the DST peak with varying mixing chamber temperature. The blue dashed line shows the saturation of the peak FWHM at low temperature.

[1] M. F. Gonzalez-Zalba, A. Saraiva, M. J. Caldern, D. Heiss, B. Koiller, and A. J. Ferguson, Nano Letters **14**, 5672 (2014).

[2] W. G. van der Wiel, S. De Franceschi, J. M. Elzerman, T. Fujisawa, S. Tarucha, and L. P. Kouwenhoven, *Reviews of Modern Physics*, **75**, 1 (2002).

[3] S. Shevchenko, S. Ashhab, and F. Nori, Phys. Rep. **492**, 1 (2010).

[4] D. M. Berns, W. D. Oliver, S. O. Valenzuela, A. V. Shytov, K. K. Berggren, L. S. Levitov, and T. P. Orlando, Phys. Rev. Lett. **97**, 150502 (2006).

[5] F. Persson, C. M. Wilson, M. Sandberg, and P. Delsing, Phys. Rev. B **82**, 134533 (2010).

[6] M. F. Gonzalez-Zalba, S. Barraud, A. J. Ferguson, and A. C. Betz, Nat. Commun. **6**, 6084 (2015).

[7] M. G. House, K. Kobayashi, B. Weber, S. J. Hile, T. F. Watson, J. van der Heijden, S. Rogge, and M. Y. Simmons, Nat. Commun. **6**, 8848 (2015).